Estimation of the number of synapses in the hippocampus and brain-wide by volume electron microscopy and genetic labeling

Andrea Santuy[1], Laura Tomás-Roca[2], José-Rodrigo Rodríguez[1,3,4], Juncal González-Soriano[5], Fei Zhu[2,6], Zhen Qiu[2], Seth GN Grant[2], Javier DeFelipe[1,3,4], Angel Merchan-Perez[1,4,7]

1 Laboratorio Cajal de Circuitos Corticales, Centro de Tecnología Biomédica, Universidad Politécnica de Madrid, Pozuelo de Alarcón, 28223 Madrid, Spain.
2 Genes to Cognition Program, Centre for Clinical Brain Sciences, University of Edinburgh, Edinburgh EH16 4SB, UK
3 Instituto Cajal, Consejo Superior de Investigaciones Científicas (CSIC), Avda. Doctor Arce, 37, 28002 Madrid, Spain.
4 Centro de Investigación Biomédica en Red sobre Enfermedades Neurodegenerativas (CIBERNED) ISCIII, Madrid, Spain.
5 Departamento de Anatomía y Embriología, Universidad Complutense de Madrid, 28040 Madrid, Spain.
6 UCL Institute of Neurology, Queen Square, WC1N 3BG London, UK
7 Departamento de Arquitectura y Tecnología de Sistemas Informáticos, Universidad Politécnica de Madrid, Pozuelo de Alarcón, 28223 Madrid, Spain. Corresponding author

JDF, SG and AMP designed research; AS, LTR, JRR, JGS, FZ and ZQ performed research; AS, LTR, and AMP analyzed data; AS, LTR, SG, JDF and AMP wrote the paper.

Abbreviated Title: Brain-wide estimation of synapses

Correspondence should be addressed to: Angel Merchan-Perez, Laboratorio Cajal de Circuitos Corticales, Centro de Tecnología Biomédica, Universidad Politécnica de Madrid, Pozuelo de Alarcón, 28223, Madrid, Spain: angel.merchan@upm.es

Abstract

We have estimated the densities of synapses per unit volume in the whole mouse brain. To do this, we combined Spinning Disc confocal Microscopy (SDM) that acquires images of synaptic proteins labeled with fluorophores in large brain areas, and FIB-SEM, a three-dimensional electron microscopy technique that provides a resolution beyond that of the confocal microscope, but in relatively small areas. The postsynaptic scaffold proteins PSD95 and SAP102 were genetically labeled to visualize excitatory synapses with SDM. We calculated the densities of synaptic puncta (with SDM) and the actual number of synapses (with FIB-SEM) in the CA1 region of the hippocampus. We then calculated the quantitative relationship between the densities of fluorescent puncta and the number of synapses. Finally, we applied this conversion factor to other regions of the brain where densities of puncta were available. We observed three different groups of brain regions, one with the highest densities of synapses (isocortex, olfactory areas, hippocampal formation and cortical subplate), a second group with low densities of synapses (pallidum, hypothalamus, brainstem and cerebellum), and a third group comprising structures which showed a wide range of synapse densities (striatum and thalamus).

Keywords

FIB-SEM, PSD95, SAP102, Hippocampus, CA1

Significance statement

Neurons communicate through synapses. Determining the number of synapses that are present in different brain regions is therefore crucial to understand brain connectivity as a whole. Here we have developed a technique that allows us to estimate the number of synapses that are present in more than one hundred regions brain-wide. We found that, in general, rostral parts of the brain —including the neocortex— have the highest numbers of synapses, while caudal regions —including the cerebellum and brainstem— have much lower numbers of synapses. Other regions, such as the thalamus, are highly heterogeneous. These quantitative data will help to better understand the structure of brain microcircuits and to build realistic whole-brain models.

Introduction

Membrane-associated guanylate kinases (MAGUKs) are a family of scaffold proteins that participate in the regulation of cell polarity, cell adhesion and synaptic signal transduction (Migaud et al., 1998; Ye et al., 2018; Zhu et al., 2016). PSD95 and SAP102 belong to the MAGUK family and are expressed in the postsynaptic density (PSD) of excitatory glutamatergic synapses (Aoki et al., 2001; Chen et al., 2018, 2008; DeGiorgis et al., 2006; Farley et al., 2015; Husi et al., 2000; Petersen et al., 2003; Valtschanoff et al., 1999; Yamasaki et al., 2016), where they contribute to the recruitment and retention of glutamate receptors (Hafner et al., 2015; Jeyifous et al., 2016; Levy et al., 2015). Genetic labeling of the endogenous PSD95 and SAP102 postsynaptic proteins and posterior imaging using Spinning Disk confocal Microsocpy (SDM) have been proven to be extremely useful for the characterization of synapse diversity in all brain regions of the mouse. High-speed SDM allows the imaging of entire brain sections and visualization of millions of synapses at a time, providing bi-dimensional densities of puncta per surface area (puncta/100 μm^2) (Zhu et al., 2018).

Previous attempts have been made to calculate the density of synapses in the brain using electron microscopy (EM). This technique allows the identification of individual synapses; however, it is restricted to much smaller fields of view. Furthermore, most of these EM studies apply stereological techniques to single EM sections. Although stereology is a proven valuable method for object counting, the total number of synapses is an estimation which is subject to several technical limitations [see (DeFelipe et al., 1999) for a review]. In the present study, we use Focused Ion Beam milling-Scanning Electron Microscopy (FIB-SEM) — an EM technique that allows the identification of all individual synapses within a known volume of brain tissue, reconstructed from serial sections. Image acquisition is fully automated, eliminating the need for manual serial sectioning, the collection of ultrathin sections, and the manual acquisition of microphotographs (Merchán-Pérez et al., 2009). Thus, although the true density of synapses per unit volume can be obtained directly (not through estimations using stereological methods), to date it has only been possible to examine relatively small 3D regions of the brain.

The aim of our study was first to obtain detailed data about the synaptic density and size of synapses in the CA1 of the hippocampus using FIB-SEM and, second, to enable both technologies —SDM and FIB-SEM— to be used in a complementary manner (Figure 1), so that the actual densities of synapses per unit volume could be estimated brainwide. We have chosen CA1 since it is a key region in the hippocampal circuitry for which the numbers of excitatory and inhibitory synapses have not been fully addressed in the mouse using volume EM. Furthermore, CA1 was used as a reference region in transgenic mice expressing fluorescence-labeled PSD95 and SAP102 to estimate the number of synapses brain-wide. To this end, we have used SDM and FIB-SEM to measure the densities of puncta and synapses, respectively, in stratum oriens (SO), stratum radiatum (SR) and stratum lacunosum-moleculare (SLM). We then calculated the quantitative relationship between the densities of puncta and synapses obtained by the two methods. This quantitative relationship or conversion factor was later applied to other regions of the brain where densities of puncta are available (Zhu et al., 2018) but no 3D electron microcopy methods have yet been applied.

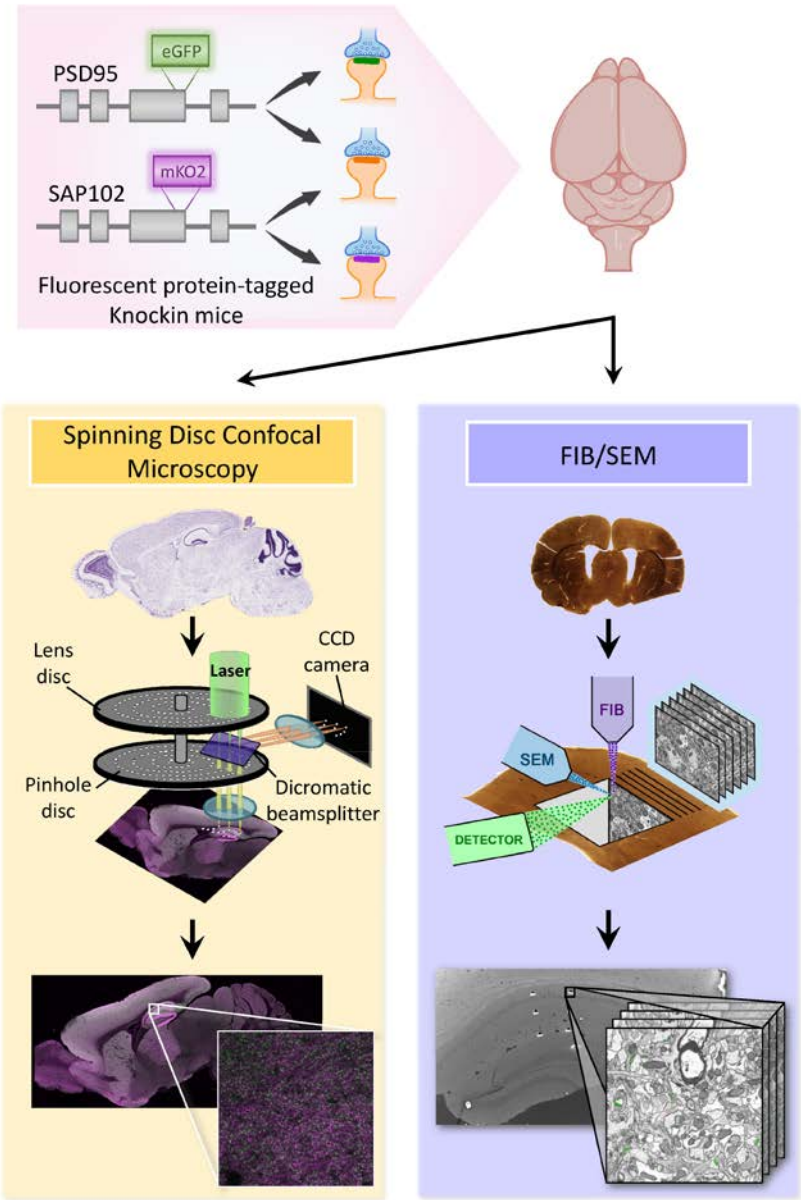

Figure 1. General methodology. Knockin mice expressing fluorescent PSD95 and SAP102 were imaged with Spinning Disc Confocal Microscopy (SDM) and with FIB-SEM. SDM allows the acquisition of large field, 2D fluorescent images, while FIB-SEM is an electron microscopy technique with a resolution in the scale of nanometres that generates 3D stacks of images, but with a smaller field of view. We have used a combination of both techniques to estimate the actual densities of synapses per unit volume brainwide.

Materials and Methods

Animals

For this study, we used adult male mice (postnatal day 56) expressing fluorescently labeled PSD95 and SAP102 postsynaptic proteins ($PSD95^{eGFP/eGFP}$; $SAP102^{mKO2/Y}$) (Zhu et al., 2018). All animals were handled in accordance with the guidelines for animal research set out in the European Community Directive 2010/63/EU, and all procedures were approved by the local ethics committee.

Tissue preparation for spinning disc microscopy

Sixteen mice were anesthetized by an intraperitoneal injection of 0.1 mL of 20% w/v sodium pentobarbital (Euthatal, Merial Animal Health Ltd. or Pentoject, Animalcare Ltd.). After complete anesthesia, 10 mL of phosphate buffered saline (PBS; Oxoid) were perfused transcardially, followed by 10 mL of 4% v/v paraformaldehyde (PFA; Alfa Aesar). Whole brains were dissected out and post-fixed for 3–4 h at 4° C in 4% PFA, and then cryoprotected for 3 days at 4 °C in 30% sucrose solution (w/v in 1× PBS; VWR Chemicals). Brains were then embedded into optimal cutting temperature (OCT) medium within a cryomould and frozen by placing the mould in isopentane cooled down with liquid nitrogen. Brains were then sectioned, with a thickness of 18 µm, using an NX70 Thermo Fisher cryostat, and cryosections were mounted on Superfrost Plus glass slides (Thermo scientific) and stored at −80 °C.

Histology and immunohistochemistry

Sections were washed for 5 min in PBS, incubated for 15 min in 1 µg/mL DAPI (Sigma), washed and mounted using home-made MOWIOL (Calbiochem) containing 2.5% anti-fading agent DABCO (Sigma-Aldrich), covered with a coverslip (thickness #1.5, VWR international) and imaged the following day.

Spinning Disk Confocal Microscopy

For synaptome mapping, we used Spinning Disk confocal Microscopy (SDM) platforms. The Andor Revolution XDi was used with an Olympus UPlanSAPO 100X oil immersion lens (NA 1.4), a CSU-X1 spinning-disk (Yokogawa) and an Andor iXon Ultra monochrome back-illuminated EMCCD camera. Images acquired with this system have a pixel dimension of 84 × 84 nm and a depth of 16 bits. A single mosaic grid was used to cover each entire brain section with an adaptive Z focus set-up by the user to follow the unevenness of the tissue using Andor iQ2 software. In both systems, eGFP was excited using a 488 nm laser and mKO2 with a 561 nm laser. The CV1000 system is equipped with the following filters: BP 525/50 nm for eGFP and BP 617/73 nm for mKO2, whereas the Andor Revolution XDi is equipped with a Quad filter (BP 440/40, BP 521/21, BP 607/34 and BP 700/45). For both systems, mosaic imaging was set up with no overlap between adjacent tiles.

Detection and measurement of fluorescent Synaptic Puncta

Punctum detection was performed using Ensemble Detection, an in-house collection of image detection algorithms. We have developed a new punctum/particle detection method based on a multi-resolution image feature detector and supervised machine learning technique (Zhu et al., 2018). In this method, we carry out a multi-resolution and multi-orientation version of 2nd-order nonlocal derivative (NLD) (Qiu et al., 2012), and use it to calculate intensity differences, referred to as ‘image features’, for each of the individual puncta at different spatial resolutions

and orientations. An initial intensity threshold is set to a very low value to only filter out extremely dim puncta and to avoid missing true synaptic puncta. The remaining candidate puncta were finally classified as either true puncta or background noise using the corresponding feature vectors and the classifier. The classifier was pre-trained with the training image set and machine learning algorithms (Qiu et al., 2012).

After detection and localization of all puncta, we segmented them based on their individual intensity values: for each punctum, a threshold was set as 10% of the maximum pixel intensity within the punctum, so that punctum size and shape measurement were independent of punctum intensity (Zhu et al., 2018). With the puncta segmented and binarized, six punctum parameters were then calculated: mean punctum pixel intensity, punctum size, skewness, kurtosis, circularity, and aspect ratio.

Tissue Preparation for electron microscopy

Four male PSD95$^{eGFP/eGFP}$; SAP102$^{mKO2/Y}$ mice were used for electron microscopy. Animals were administered a lethal intraperitoneal injection of sodium pentobarbital (40 mg/kg) and were intracardially perfused with 2% paraformaldehyde and 2.5% glutaraldehyde in 0.1 M phosphate buffer (PB). The brain was then extracted from the skull and processed for EM as previously described (Merchán-Pérez et al., 2009). Briefly, the brains were post-fixed at 4°C overnight in the same solution used for perfusion. They were then washed in PB and vibratome sections (150 µm thick) were obtained. Sections containing the rostral hippocampus were selected with the help of an atlas (Paxinos and Franklin, 2004). Selected sections were osmicated for 1 hour at room temperature in PB with 1% OsO4, 7% glucose and 0.02 M $CaCl_2$. After washing in PB, the sections were stained for 30 min with 1% uranyl acetate in 50% ethanol at 37°C, and they were then dehydrated and flat embedded in Araldite (DeFelipe and Fairén, 1993). Embedded sections were glued onto blank Araldite stubs and trimmed. To select the exact location of the samples, we first obtained plastic semithin sections (1–2 µm thick) from the block surface and stained them with toluidine blue to identify cortical layers. These sections were then photographed with a light microscope. The last of these light microscope images (corresponding to the section immediately adjacent to the block face) was then collated with scanning electron microscope (SEM) photographs of the surface of the block. In this way, it was possible to accurately identify the regions of the neuropil to be studied.

Three-Dimensional Electron Microscopy

Three-dimensional brain tissue samples of the CA1 of the hippocampus were obtained using combined focused ion beam milling and scanning electron microscopy (FIB-SEM) (Figure 2). The focus of our study was the neuropil, which is composed of axons, dendrites and glial processes. We used a CrossBeam 540 electron microscope (Carl Zeiss NTS GmbH, Oberkochen, Germany). This instrument combines a high-resolution field emission SEM column with a focused gallium ion beam, which can mill the sample surface, removing thin layers of material on a nanometer scale. After removing each slice (20 nm thick), the milling process was paused, and the freshly exposed surface was imaged with a 1.8-kV acceleration potential using the in-column energy selective backscattered (EsB) electron detector. The milling and imaging processes were sequentially repeated, and long series of images were acquired through a fully automated procedure, thus obtaining a stack of images that represented a three-dimensional sample of the tissue (Merchán-Pérez et al., 2009). Twelve samples (stacks of images) of the neuropil of three strata of CA1 were obtained, avoiding the neuronal and glial somata as well as the blood vessels (Figure 3). These stacks included four samples of stratum lacunosum

208 moleculare (SLM), four of stratum radiatum (SR) and four of stratum oriens (SO) (see
209 Supplementary Table 1). In these stacks, we obtained the densities of glutamatergic
210 (asymmetric) and GABAergic (symmetric) synaptic junctions. To do this, we counted the
211 number of synaptic junctions within an unbiased three-dimensional counting frame of known
212 volume (Howard and Reed, 2005). Image resolution in the xy plane was 5 nm/pixel; resolution
213 in the z-axis (section thickness) was 20 nm and image sizes were 2048 x 1536 pixels. The
214 number of sections per stack ranged from 201 to 377 (mean 276.33; total 3316 sections).
215 Processing for EM causes shrinkage of the tissue for which we have to correct the
216 measurements (Merchán-Pérez et al., 2009). Correction factors were 0.9508 for linear
217 measurements, 0.9040 for area measurements and 0.8595 for volumetric data. The volumes of
218 the stacks, after correction for tissue shrinkage, ranged from 367.81 to 689.86 μm^3 (mean
219 505.66 μm^3; total 6067.86 μm^3). The volumes of the counting frames ranged from 288.62 to
220 585.99 μm^3 (mean 408.76 μm^3; total 4905.07 μm^3) (Supplementary Table 1).

221 **Identification and reconstruction of synapses**

222 Synaptic junctions within these volumes were visualized and segmented in 3D with Espina
223 software (Morales et al., 2011)(http://cajalbbp.es/espina/). The segmentation algorithm
224 makes use of the fact that presynaptic and postsynaptic densities appear as dark, electron-
225 dense structures under the electron microscope. It requires a Gaussian blur filter
226 preprocessing to eliminate noisy pixels and then it uses a gray-level threshold to extract all the
227 voxels that fit the gray levels of the synaptic junction. In this way, the resulting 3D
228 segmentation includes both the active zone (AZ) and postsynaptic density (PSD) (Morales et
229 al., 2013). Synaptic junctions with a prominent or thin PSD were classified as asymmetric or
230 symmetric synaptic junctions, respectively (Figure 2). Synapses could be unambiguously
231 identified since they can be visualized in consecutive serial sections and, if necessary, they can
232 be digitally resectioned in different planes to ascertain their identity as asymmetric or
233 symmetric synapses (DeFelipe et al., 1999; Merchán-Pérez et al., 2009).

234 **Size of synapses**

235 As stated above, the synaptic junction is formed by the AZ and the PSD. Since AZ and PSD are
236 in close apposition and have similar surface areas, they can be represented as a single surface
237 — the synaptic apposition surface (SAS). Thus, the SAS is an accurate measurement of the size
238 of the synapse. In previous studies we have developed an efficient computational technique to
239 automatically extract this surface from reconstructed synapses (Morales et al., 2013).

240 **Statistical analysis**

241 To study whether there were significant differences between synaptic distributions among the
242 different CA1 layers, we performed a multiple mean comparison test. When the data met the
243 criteria of normality and homoscedasticity, an ANOVA was performed. When these criteria
244 were not met, we used the Kruskal-Wallis followed by Dunn's test for pair-wise comparisons.

245

246

Results

We estimated the density and the size of synapses with two alternative methods (Figure 1). PSD95-positive synapses were identified as fluorescent puncta using SDM, and FIB-SEM was used to visualize and reconstruct synaptic junctions in the same regions, so the estimations made with confocal microscopy could be validated. EM also provided information that was not obtained in confocal images, such as the relative proportions of excitatory (asymmetric) and inhibitory (symmetric) synapses (Figure 2, Figure 3).

Density of PSD95/SAP102 puncta and synapses

Densities of fluorescent puncta (number of positive puncta per 100 μm^2) were measured in SLM, SR and SO from CA1. We obtained the densities of puncta expressing PSD95 (*dPSD95*), SAP102 (*dSAP102*) and the colocalization index (*c*). The colocalization index ranges from 0, when there is no colocalization, to 1, when there is 100% colocalization. From these data we calculated the total density of puncta (*dTotal*) (Table 1). Note that the total density of puncta is not simply the sum of *dPSD95* and *dSAP102*, since there is a certain density of puncta that colocalize (*dColoc*). We operated as follows:

$$dTotal = dPSD95 + dSAP102 - dColoc$$

$$dColoc = c \times dTotal$$

therefore,

$$dTotal = \frac{dPSD95 + dSAP102}{1 + c}$$

We observed the highest puncta density in SR (mean ± SD; 147.30 ± 27.49 puncta/100 μm^2), followed by SO (141.13 ± 17.39 puncta/100 μm^2) and SLM (104.46 ± 23.57 puncta/100 μm^2). The differences between SLM and the other two layers were statistically significant (KW test, $p < 0.005$) (Figure 4A).

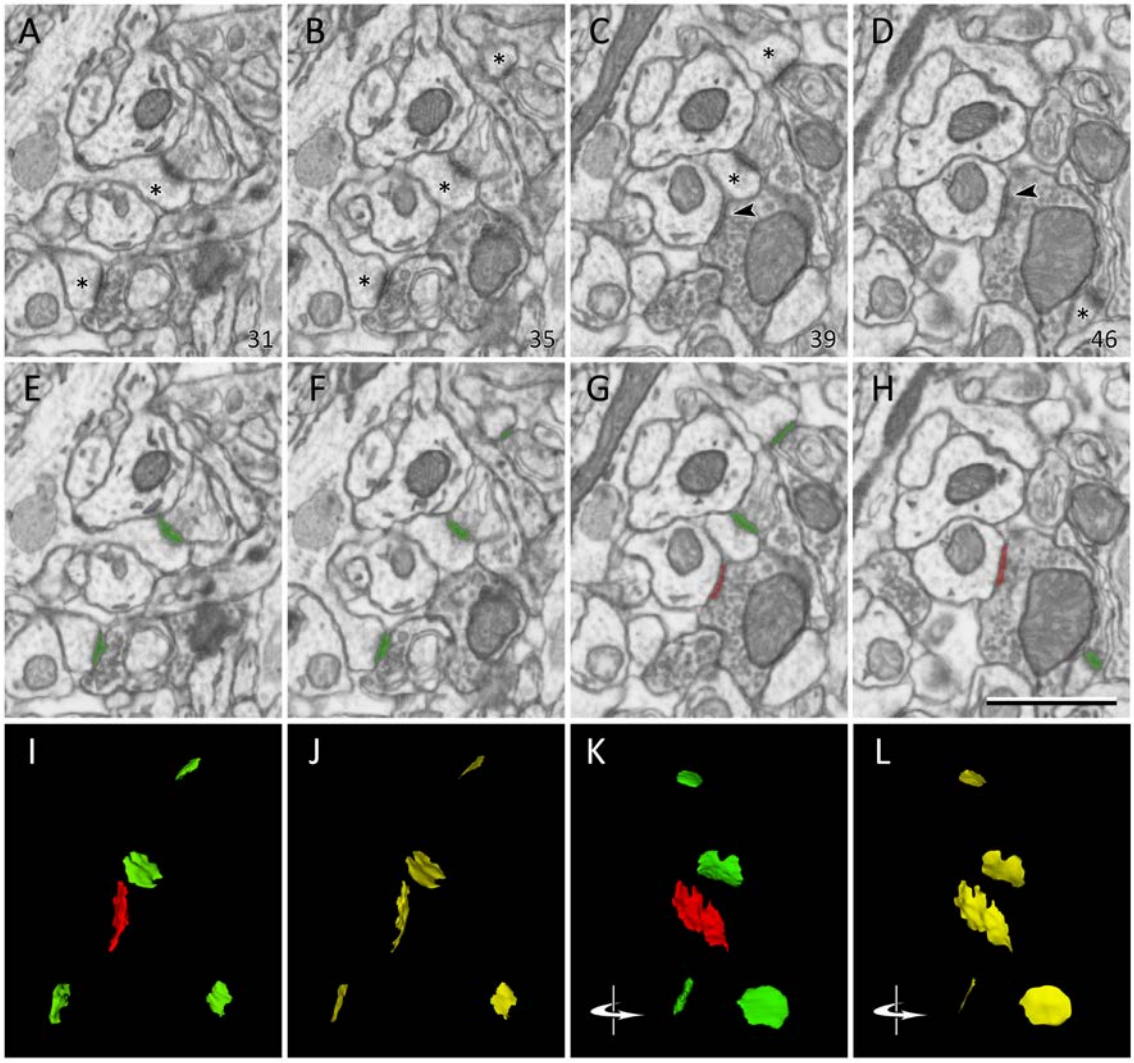

Figure 2. Identification and segmentation of synaptic junctions in serial sections acquired by FIB-SEM. (A-C) Detail of four electron micrographs selected from a series o images obtained by FIB-SEM. In this example, the stack of images was obtained from the stratum oriens. The numbers in the bottom-right corner correspond to section number. Four asymmetric synapses can be identified by the presence of prominent post-synaptic densities in A, B, C and D (asterisks). One symmetric synapse, with a thin post-synaptic density, can be seen in C and D (arrow heads). Note that the classification of synapses as asymmetric or symmetric is not based on single images but on the examination of the full sequence of images. **(E-H)** The same images after they have been segmented with Espina software (http://cajalbbp.es/espina/). The segmentation process is based on grey-level thresholds, so the resulting 3D objects comprise both the pre- and post-synaptic densities (see methods). Green profiles correspond to asymmetric synapses and red profiles to the symmetric synapse. **(I)** 3D rendering of the synaptic junctions present in A to H. **(J)** Synaptic apposition surfaces (SAS, yellow) extracted from the 3D segmentations represented in (I). SAS are automatically extracted from the 3D reconstructions of synaptic junctions (see methods); they are zero-volume surfaces that represent the interface between the pre- and post-synaptic densities. The surface area of the SAS is measured for each individual synaptic junction. **(K, L)** Same structures represented in I and J, respectively, after they have been rotated through a vertical axis. Original images were acquired with a resolution of 5 nm/pixel, with a distance of 20 nm between two consecutive images. Calibration bar in H is 1 µm.

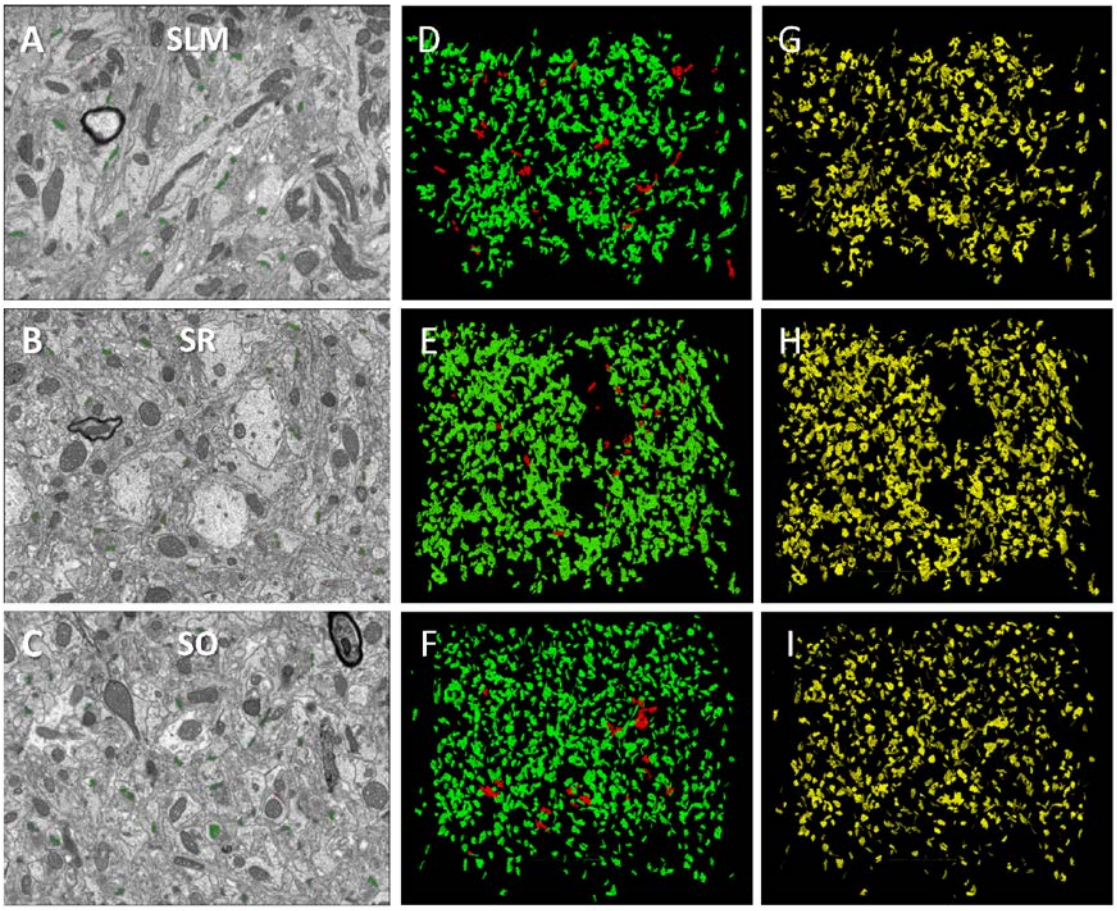

Figure 3. Measuring synaptic densities and sizes in stacks of sections obtained by FIB-SEM. (A-C) Panoramic view of electron micrographs of the stratum lacunosum moleculare (SLM), stratum radiatum (SR) and stratum oriens (SO) imaged by FIB-SEM. **(D-F)** 3D rendering of synaptic junctions reconstructed from the corresponding stacks of serial sections, acquired from the strata represented in A to C. Asymmetric synaptic junctions have been represented in green and symmetric synaptic junctions in red. **(G-I)**. The synaptic apposition surfaces (SAS, yellow) have been automatically extracted from the three-dimensionally reconstructed synaptic junctions. The number of synapses per unit volume and the surface areas of the SAS have been measured in each stack of serial sections (see Tables 1 and 2).

301 For the volume electron microscopy study, we used 12 stacks of serial sections from SLM, SR
302 and SO. In these samples, we identified and analyzed a total of 10,460 synapses in 4,905 μm^3
303 of tissue. Of these, 95.60% were AS and 4.40% were SS. To estimate the density of synapses in
304 each stack of images, we counted the number of synaptic junctions within an unbiased three-
305 dimensional counting frame of known volume (see Methods). The density of AS (mean ± SD) in
306 SLM was 1.59 ± 0.73 synapses/μm^3, in SR it was 2.31 ± 0.38 synapses/μm^3, and in SO it was
307 2.49 ± 0.48 synapses/μm^3 (Table 1). SS were most frequent in SLM (0.13 ± 0.07 synapses/μm^3),
308 followed by SR (0.06 ± 0.02 synapses/μm^3) and SO (0.05 ± 0.02 synapses/μm^3). In spite of this
309 trend of an increase in AS density from SLM to SO, and a decrease in SS across these strata, the
310 differences between layers were not statistically significant for either the total density of
311 synapses (AS+SS) or for AS and SS separately (KW test, $p \geq 0.08$) (Figure 4B, C).

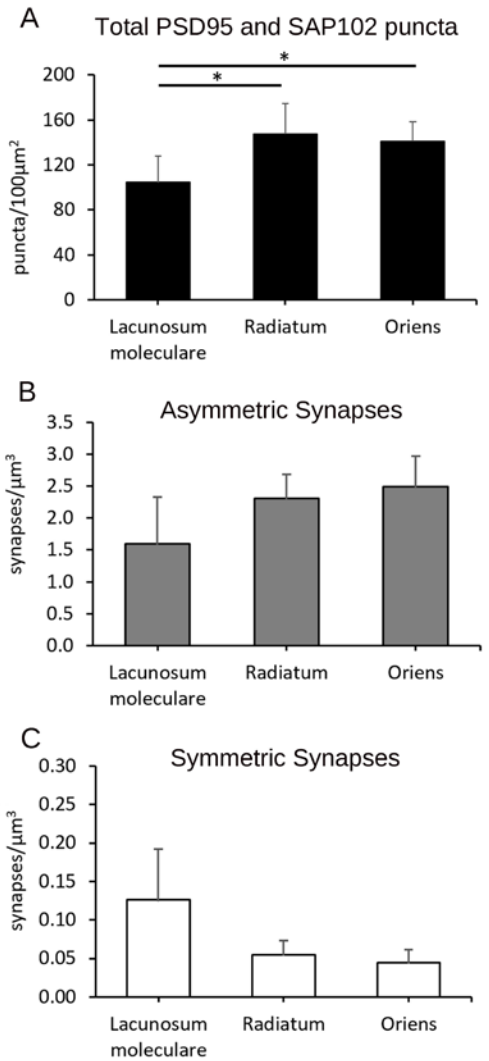

312 **Figure 4. Total densities of PSD95 and SAP102 puncta, asymmetric synapses and symmetric**
313 **synapses.** (**A**) Density of PSD95- and SAP102-positive puncta (puncta/100 μm^2 ± SD) acquired
314 by SDM in the hippocampus (CA1). Asterisks indicate statistically significant differences (KW, p
315 < 0.005). (**B)** and **(C)** Density of asymmetric and symmetric synapses, respectively
316 (synapses/μm^3 ± SD), estimated from stacks of serial sections acquired by FIB-SEM from the
317 same region.

When we compared SDM and FIB-SEM data, we found that both methods revealed lower densities in SLM and higher and similar densities in SR and SO. We then calculated a conversion factor that would allow us to relate the densities of PSD95 and SAP102 puncta to the actual densities of excitatory synapses found by FIB-SEM. These conversion factors were calculated as the quotient between the actual density of excitatory synapses and total density of PSD95 and SAP102 puncta (Table 1). Conversion factors obtained for each layer of CA1 were slightly different; they ranged from 0.0152 to 0.0176. As a conservative approach, we also calculated an averaged conversion factor with data from the three layers analyzed (Table 1).

Stratum of CA1	**Density of PSD95** (puncta/100 μm^2)	**Density of SAP102** (puncta/100 μm^2)	**Coloca-lization index**	**Total density of puncta/100 μm^2**	**Density of AS** (synapses/ μm^3)	**Conver-sion factor**
Lacunosum-Moleculare	86.9174 ± 19.1856	79.5983 ± 26.1547	0.5973	104.4573 ± 23.5698	1.5958 ± 0.7317	0.0153
Radiatum	122.9793 ± 25.4202	121.0397 ± 22.3355	0.6607	147.3026 ± 27.4920	2.3076 ± 0.3788	0.0157
Oriens	121.1208 ± 19.1566	111.7809 ± 17.4686	0.6520	141.1321 ± 17.3944	2.4887 ± 0.4763	0.0176
All layers averaged	110.3392 ± 26.8614	104.1396 ± 28.2323	0.6367	130.9640 ± 29.6704	2.1307 ± 0.6396	0.0162

Table 1. Relationship between the densities of puncta and the densities of synapses. PSD95 and SAP102 puncta were imaged with SDM. The total densities of puncta were calculated from the densities of PSD95 and SAP102 puncta, together with the colocalization index (see text for details). The densities of asymmetric synapses (AS) were obtained from volumes of tissue reconstructed from serial sections using FIB-SEM. For each layer, the conversion factors is the quotient between the density of synapses obtained by FIB-SEM and the total density of puncta calculated from SDM images. Densities are given as average ± SD.

The next step was to calculate the total number of puncta expressing PSD95 and/or SAP102 brain-wide, using previously published data (Supplementary Table 2). These data are available for 12 major brain regions divided into 113 subregions (Zhu et al., 2018). Our analysis indicates that brain regions can be classified into three groups according to the different combinations of densities of PSD95, SAP102 and total densities of puncta (Figure 5). The first group shows the highest total densities of puncta; it includes the isocortex, the olfactory areas, the hippocampal formation and the cortical subplate. All these regions are relatively homogeneous except the hippocampal formation, which shows wider ranges of variability. Also, isocortical areas show a relatively higher proportion of PSD95 versus SAP102 than the other regions. A second group is formed by regions that show low densities of puncta; these regions are the pallidum, the hypothalamus, the brainstem and the cerebellum. Finally, the third group is formed by structures whose components range from low to high densities of puncta. This group includes the striatum and especially the thalamus, which shows the highest range of variability. For example, of all thalamic nuclei, the ventral medial nucleus had one of the lowest estimated densities of total puncta (19.78 puncta/100 μm^2), while the posterior

complex had one of the highest estimated densities (110.15 puncta/100 µm^2) (Supplementary Table 2). As a validation step, we compared previously published data regarding CA1 (Zhu et al., 2018) with our present data; the total densities of puncta expressing PSD95 and/or SAP102 were remarkably similar (128.95 puncta/100µm^2 in previously published data and 130.96 puncta/100µm^2 in the present study).

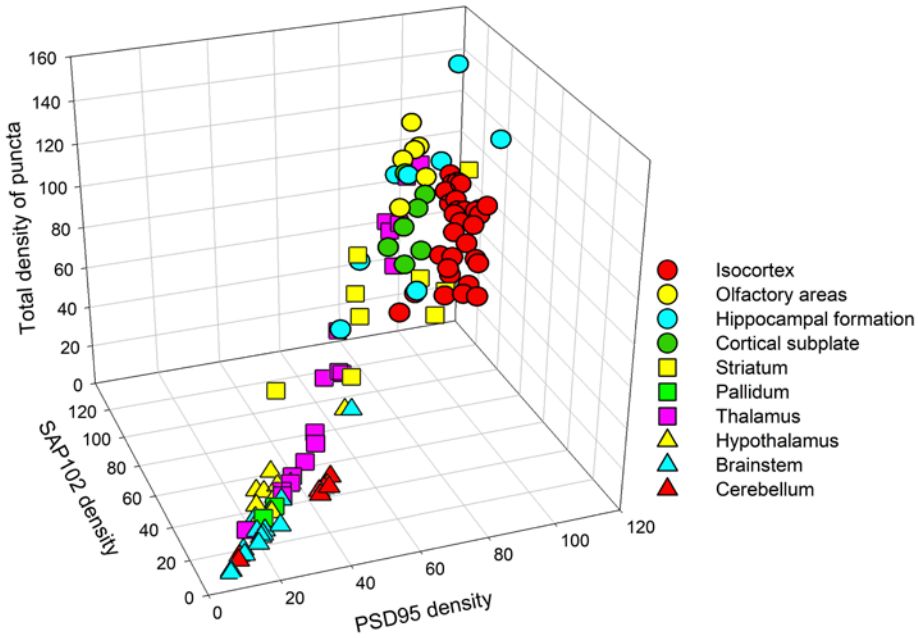

Figure 5. Densities of PSD95 and SAP102 puncta, and total densities of puncta in different regions of the brain. The total densities of puncta have been calculated from previously published colocalization indexes and densities of PSD95 and SAP102 puncta (Zhu et al., 2018). Brain regions can be classified into three groups. The first group shows the highest total densities of puncta; it includes the isocortex, the olfactory areas, the hippocampal formation and the cortical subplate. A second group shows low densities of puncta; these regions are the pallidum, the hypothalamus, the brainstem and the cerebellum. The third group is formed by structures with densities of puncta ranging from low to high, and includes the striatum and thalamus.

Finally, we estimated the actual density of synapses expressing PSD95 and/or SAP102, making use of the averaged conversion factor obtained in CA1 (0.0162, see Table 1). The values obtained have been graphically represented in Figure 6. In general, the hippocampal cornu ammonis, the isocortex and the olfactory areas show the highest synaptic densities, intermingled with cortical subplate nuclei. Within the hippocampal formation, the dentate gyrus and the subiculum presented similar densities, but they were lower than in the Ammon's horn. Striatal nuclei showed considerable variations, but the thalamic nuclei showed the highest variability, as mentioned above. The cerebellar cortex showed homogeneously low densities and the pallidum, hypothalamus and brainstem had the lowest synaptic densities.

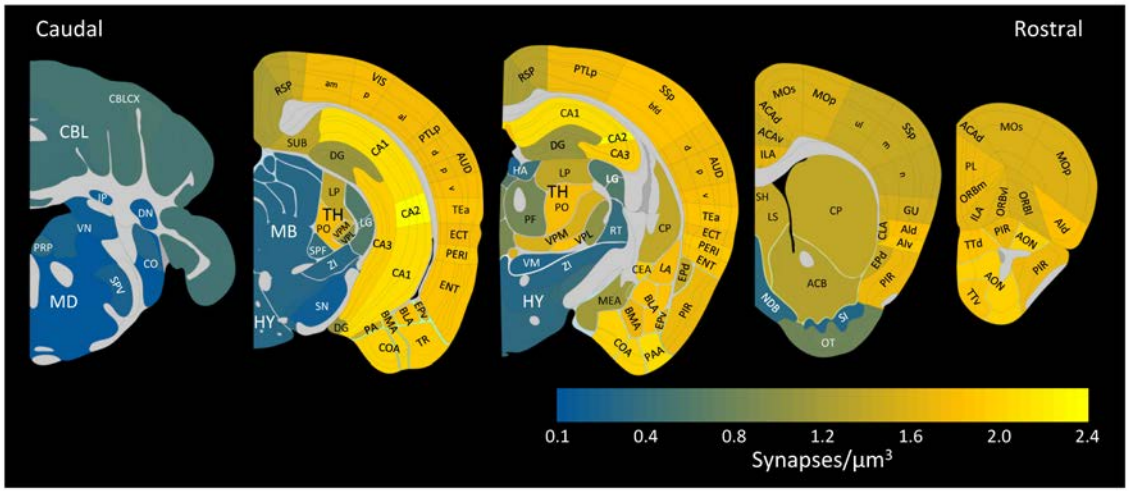

Figure 6. Estimated densities of synapses expressing PSD95 and/or SAP102 in different regions of the brain. The total densities of puncta have been calculated from previously published densities of PSD95 and SAP102, as well as their colocalization indexes (Zhu et al., 2018). A conversion factor obtained in CA1 was used to estimate the actual densities of synapses per cubic micron (see text for details). Illustrations and brain regions are based on the Allen Mouse Brain Atlas. The following structures have been labeled: **Cerebellum** (CBL), CBLCX: cerebellar cortex; DN: Dentate nucleus; IP: Interposed nucleus. **Medulla** (MD), CO: Cochlear nuclei; PRP: Nucleus prepositus; SPV: Spinal nucleus of the trigeminal; VN: Vestibular nuclei. **Midbrain** (MB), SN: Substantia nigra. **Hypothalamus** (HY), ZI: Zona incerta. **Thalamus** (TH), HA: Habenular nuclei; LG: Lateral geniculate complex; LP: Lateral posterior nucleus; PF: Parafascicular nucleus; PO: Posterior complex; RT: Reticular nucleus; SPF: Suprafascicular nucleus; VM: Ventral medial nucleus; VPL: Ventral posterolateral nucleus; VPM: Ventral posteromedial nucleus. **Pallidum**, NDB: Diagonal band nucleus; SI: Substantia innominata. **Striatum**, ACB: Nucleus accumbens; CEA: Central amygdalar nucleus; CP: Caudoputamen; LS: Lateral septal nucleus; MEA: Medial amygdalar nucleus. OT: Olfactory tubercle; SH: septohippocampal nucleus. **Cortical subplate**, BLA: Basolateral amygdalar nucleus; BMA: Basomedial amygdalar nucleus; CLA: Claustrum; EPd: Endopiriform nucleus, dorsal part; EPv: Endopiriform nucleus, ventral part; LA: Lateral amygdalar nucleus; PA: Posterior amygdalar nucleus. **Olfactory areas**, AON: Anterior olfactory nucleus; COA: Cortical amygdalar area; PAA: Piriform-amygdalar area; PIR: Piriform area; TR: Postpiriform transition area; TTd: Taenia tecta, dorsal part; TTv: Taenia tecta, ventral part. **Hippocampal formation**, CA1, CA2, CA3: Cornu Ammonis, fields 1, 2 and 3; DG: Dentate gyrus. ENT: Entorhinal area; SUB: Subiculum. **Isocortex**, ACAd: Anterior cingulate area, dorsal part; ACAv: Anterior cingulate area, ventral part; AId: Agranular insular area, dorsal part; AIv: Agranular insular area, ventral part; AUD: Auditory areas (d, p, v: dorsal, primary ventral); ECT: Ectorhinal area; GU: Gustatory area; ILA: Infralimbic area; MOp: Primary motor area; MOs: Secondary motor area; ORBl: Orbital area, lateral part; ORBm: Orbital area, medial part; ORBvl: Orbital area, ventrolateral part; PERI: Perirhinal area; PL: Prelimbic area; PTLp: Posterior parietal association areas; RSP: Retrosplenial area; SSp: Primary somatosensory area (bfd, ul m, and n: barrel field, upper limb, mouth and nose representations); TEa: Temporal association areas; VIS: Visual areas (am, p, al: anteromedial, primary, anterolateral).

410 **Size of synapses**

411 We measured the area of PSD95 puncta in SLM, SR and SO. The largest mean area of puncta
412 was found in SLM (0.0832 μm^2), followed by SR (0.0809 μm^2) and SO (0.0798 μm^2). Although
413 the differences were small, they were statistically significant (KW test $p < 0.001$).

414 To estimate the size of synapses in the FIB-SEM samples, we measured the area of the synaptic
415 apposition surface (SAS). The SAS is a surface that represents the apposition between the
416 presynaptic density and the PSD and reproduces their curvature (see Methods). The mean SAS
417 area in the FIB-SEM samples was 0.0474 μm^2 for asymmetric synapses and 0.0541 μm^2 for
418 symmetric synapses.

419 For asymmetric synapses, the mean SAS area in SLM was larger than in the other layers
420 (0.0633 μm^2; KW-Dunn's $p < 0.001$). Despite the mean SAS area being larger in SR than in SO
421 (0.0456 μm^2 and 0.0419 μm^2, respectively), the difference was not statistically significant (KW-
422 Dunn's $p > 0.05$). For symmetric synapses, the largest mean SAS areas were found in SO
423 (0.0644 μm^2) followed by SLM (0.0519 μm^2) and SR (0.0501 μm^2) (KW, $p = 0.05$) (Figure 7,
424 Table 2).

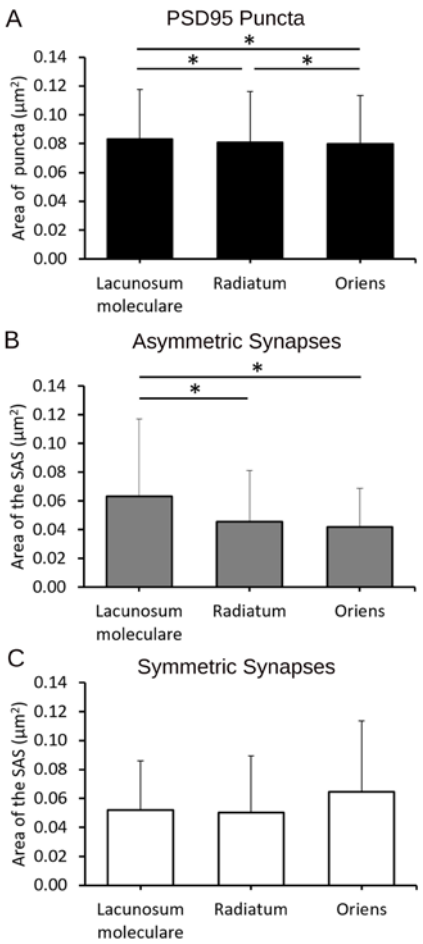

425 **Figure 7. Size of PSD95 puncta, asymmetric synapses and symmetric synapses. (A)** Area of PSD95-
426 positive puncta (μm^2) acquired by SDM in the hippocampus (CA1) (Mean + SD). Asterisks indicate
427 statistically significant differences. (**B) and (C)** Mean size of the synaptic apposition surface (SAS) of
428 asymmetric and symmetric synapses (μm^2) estimated from stacks of serial sections acquired by FIB-SEM
429 from the same region. See also Table 2.

430

When we compared the sizes of asymmetric synapses and symmetric synapses in different layers, we found that symmetric synapses were larger than asymmetric synapses in SO and SR, while in SLM the opposite was the case. The greatest differences were found in SO, where mean SAS areas for symmetric synapses and asymmetric synapses were in a proportion of approximately 6:4 (MW test, $p < 0.0001$) (Table 2).

To further characterize the size distribution of synaptic sizes, we plotted the frequency histograms of the areas of PSD95 puncta and of the SAS (Figure 8). The frequency histograms of the areas of PSD95 puncta showed skewed shapes, with a long tail to the right. The histograms of SAS areas of asymmetric synapses measured from FIB-SEM reconstructions also showed skewed shapes, but they were narrower and lay to the left of PSD95 histograms in all layers (Figure 8).

We then performed goodness-of-fit tests to find the theoretical probability density functions that best fitted the empirical distributions of the areas of PSD95 puncta and SAS areas. We found that they fitted to log-normal distributions in all cases, with some variations in the parameters μ and σ (Table 2 and Figure 8).

		Stratum			
		Lacunosum-Moleculare	Radiatum	Oriens	All layers
PSD 95 Puncta	Mean Area ± SD (μm^2)	0.0832 ± 0.0342	0.0809 ± 0.0352	0.0798 ± 0.0336	0.0813 ± 0.0342
	n	147776	189945	125916	463637
	μ	11.24	11.20	11.20	11.21
	δ	0.44	0.48	0.46	0.46
AS	Mean SAS Area ± SD (μm^2)	0.0633 ± 0.0540	0.0456 ± 0.0358	0.0419 ± 0.0271	0.0474 ± 0.0377
	n	2258	4538	5082	11878
	μ	10.74	10.55	10.50	10.54
	δ	0.80	0.63	0.57	0.64
SS	Mean SAS Area ± SD (μm^2)	0.0520 ± 0.0338	0.0501 ± 0.0394	0.0644 ± 0.0491	0.0541 ± 0.389
	n	247	93	87	427
	μ	10.67	10.60	10.97	10.70
	δ	0.68	0.65	0.75	0.69

Table 2. Surface areas of PSD95 puncta acquired by SDM, and surface areas of the synaptic apposition surface (SAS) of asymmetric (AS) and symmetric (SS) synapses reconstructed from FIB-SEM samples. The number of puncta or synapses analyzed (n), as well as the parameters μ and σ of the corresponding best-fit log-normal distributions are also indicated.

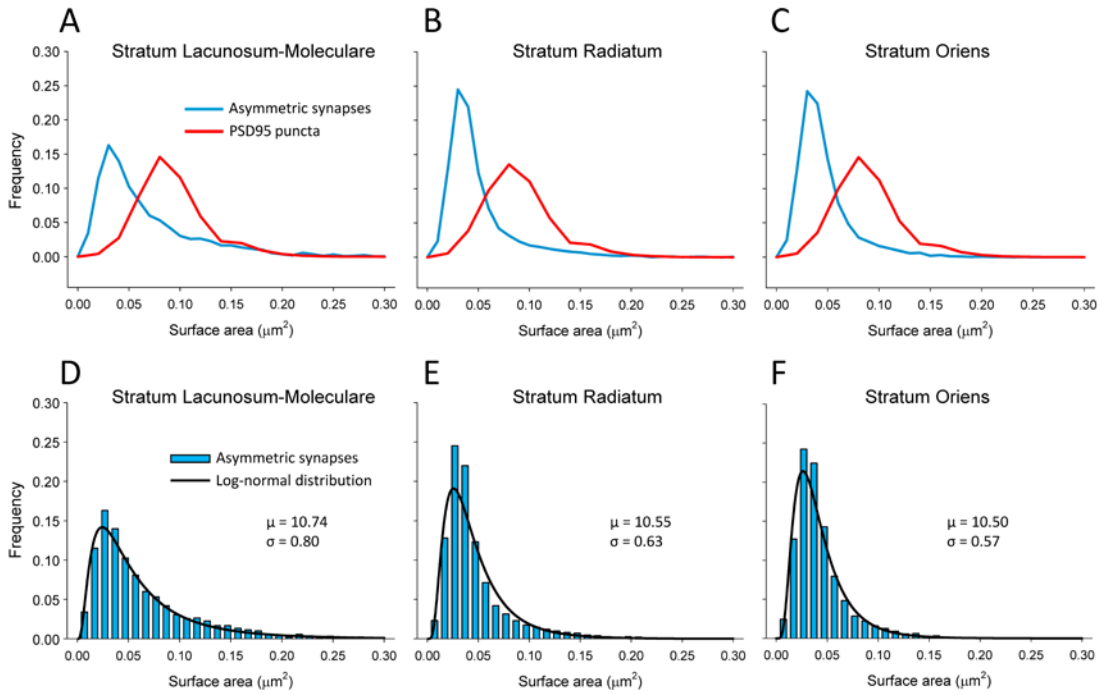

Figure 8. Frequency histograms of the sizes of PSD95 puncta and asymmetric synapses. (**A-C**) Comparison of the distribution of the surface areas of PSD95 puncta acquired by SDM (red line) and the synaptic apposition surfaces of asymmetric synapses reconstructed from FIB-SEM samples (blue line) from three layers of the CA1 region of the hippocampus. The histograms corresponding to asymmetric synapses are narrower and lie to the left of the histograms corresponding to PSD95 puncta. (**D-F)** Frequency histograms (blue bars) of the areas of the synaptic apposition surfaces of asymmetric synapses reconstructed from FIB-SEM samples. The log-normal distributions (black lines) represent the theoretical probability density functions that best fit the experimental data. The parameters μ and σ of the corresponding log-normal distributions have also been indicated.

Discussion

Relationship between the densities of puncta expressing PSD95 and/or SAP102 and the actual density of synapses

In this study, we have —for the first time— analyzed the synaptic density of excitatory and inhibitory synapses, as well as their size, in stratum oriens, stratum radiatum and stratum lacunosum-moleculare of the CA1 hippocampal region of the mouse, using three-dimensional electron microscopy. With this method, long series of consecutive sections are obtained by FIB-SEM, so individual synapses can be unambiguously identified and the number of synapses per unit volume can be directly calculated. However, as with any other electron-microscopy technique, FIB-SEM can only be applied to relatively small regions of tissue, so it is not practical for brain-wide estimations. By contrast, the number of fluorescent puncta expressing PSD95 and/or SAP102 can be quantified brain-wide using SDM, so we have attempted to establish a correlation between the two kinds of measurements.

Synapses expressing PSD95 and/or SAP102 can be quantified brain-wide but they are certainly not the only synapses that are present in any given brain region. The clearest example would be inhibitory synapses, represented by symmetric or type 2 synapses (Colonnier, 1968; Gray,

480 1959), that can be identified in FIB-SEM images because of their thin PSD (Merchán-Pérez et
481 al., 2009). In our CA1 samples, symmetric synapses represent 4.4% of the total number of
482 synapses. These do not express PSD95 or SAP102, so their densities cannot be estimated from
483 previous or present SDM data.

484 If only excitatory glutamatergic synapses express PSD95 and/or SAP102, the next question is
485 whether all excitatory synapses express these scaffold proteins. This question does not have a
486 simple answer since there have been several —often conflicting— reports and, on occasion,
487 only qualitative estimations have been provided. For example, PSD95 was regarded as "a
488 fundamental structural component of most, if not all, excitatory PSDs isolated from the rat
489 cerebral cortex" (Petersen et al., 2003). Other reports seem to confirm this view using
490 immunogold techniques. For example, in a small sample from the juvenile and adult rat
491 forebrain, 31 out of 32 PSDs analyzed showed PSD95 immunolabeling (Swulius et al., 2010)
492 and similar results were obtained in the cerebral cortex of the adult rat (DeGiorgis et al., 2006).
493 Lower percentages of PSD95-expressing synapses have been reported in the adult rat visual
494 cortex, where more than 60% of PSDs had PSD95 labeling (Aoki et al., 2001). Also, in the rat
495 hippocampus, 48% of synapses expressed PSD95 on postnatal day 35 and 45% at 6 months of
496 age (Sans et al., 2000). These lower percentages could be due to different labeling techniques.
497 Indeed, the lower percentages of PSD95 expression were questioned by a study reporting that
498 in the olfactory bulb 95–100% of synaptic profiles were immunolabeled, using a more sensitive
499 method and a higher titer of antibodies (Sassoé-Pognetto et al., 2003). In fact, this study
500 revealed an average number of immunogold particles that was five to ten times higher than
501 that previously reported in the rat hippocampus (Sans et al., 2000). Alternatively, the
502 differences could be due to actual differences in the expression of PSD95, SAP102 and other
503 proteins [see, for example (Farley et al., 2015)]. In any case, the high variability in the
504 estimations of the number of synapses expressing PSD95 or SAP102 by immunogold methods
505 might depend on the antibodies, titers and immunocytochemical techniques used. However,
506 the advantage of our genetic labeling technique is that 100% of PSD95 and SAP102 are labeled,
507 so a more reliable detection throughout the brain would be expected.

508 Turning to the adult mouse hippocampus, it has been recently claimed that all Schaffer
509 collateral/commissural synapses in the SR of CA1 show immunogold staining for PSD95
510 (Yamasaki et al., 2016). This is probably an overestimate, since our own data indicate that
511 there is a population of synapses that express SAP102 but not PSD95 (Supplementary Table 2).
512 Thus, if we consider that Schaffer collateral/commissural fibers are the origin of the vast
513 majority of synapses in SR and SO, we can assume that most, if not all, synapses in these strata
514 express PSD95, SAP102 or a combination of the two. It is likely to be the same case in SLM,
515 since the relationship between the number of fluorescent puncta and the actual density of
516 synapses measured by FIB-SEM is very similar to that of the other two layers (see Table 1).
517 Therefore, data on densities of fluorescent puncta and synapses are self-consistent and, as a
518 consequence, the calculated conversion factors between the two kinds of densities are very
519 similar in the three CA1 layers studied.

520 However, even if we assume that the vast majority of excitatory synapses in CA1 express
521 PSD95 and/or SAP102, and that we can detect them all with SDM and FIB-SEM, the question
522 remains as to whether this would be the case in other brain regions. The abundance of some
523 of the MAGUK scaffold proteins like PSD95 and SAP102 is differentially distributed through the
524 brain (Roy et al., 2018; Zhu et al., 2018). Therefore, this question is pertinent since we have
525 applied a single conversion factor, calculated in CA1, to the whole brain, and the meaning of

526 the synaptic densities that we obtain will depend on the initial assumptions. In our opinion,
527 there are two alternative possibilities. First, we can assume that all excitatory synapses in any
528 region of the brain express PSD95 and/or SAP102. This would be very similar to CA1 and so the
529 synaptic densities that we have estimated would approximately correspond to the actual
530 synaptic densities. The second possibility is that there are excitatory synapses that do not
531 express PSD95 or SAP102, and the proportion of these kinds of synapses is different in
532 different brain regions. In this case, the conversion factor would yield the densities of PSD95-
533 /SAP102-expressing synapses only, and the total density of excitatory synapses would be
534 higher, but unknown. Therefore, to interpret our results conservatively, we must assume that
535 our estimations of synaptic densities may underestimate the actual number of excitatory
536 synapses. In other words, our estimations represent the lower boundary of the densities of
537 excitatory synapses in different brain regions, since only puncta expressing PSD95 and/or
538 SAP102 have been considered, and we cannot rule out the possibility that other kinds of
539 excitatory synapses exist.

540 Only a systematic exploration of the different regions of the brain with FIB-SEM or similar
541 methods will settle the possible discrepancies between our present estimations and the actual
542 values. However, we can compare our estimations with previous studies, when available. In
543 the hippocampus, for example, previous studies in the rat SR reported 2.2 synapses/μm^3 using
544 three-dimensional reconstructions (Mishchenko et al., 2010), and similar estimates using
545 stereological methods (Sorra et al., 1998). In both cases, the reported synapse densities were
546 slightly lower than the density we have found in the same stratum of the mouse (2.4
547 synapses/μm^3). These differences in the mean synaptic densities may be attributed to
548 differences between species, although we cannot rule out the possibility of other sources of
549 bias such as the different methods used. In the mouse neocortex, previously reported synaptic
550 densities using different stereological methods were either lower (Sadaka et al., 2003; Schüz
551 and Palm, 1989) or higher (DeFelipe et al., 1997) than our present estimations. In the juvenile
552 rat somatosensory cortex, the mean density of synapses in the neuropil has been reported to
553 be between 0.87 and 0.89 synapses/μm^3 using FIB-SEM (Anton-Sanchez et al., 2014; Santuy et
554 al., 2018a), which is below our present estimation for the adult mouse somatosensory cortex
555 (1.4 to 1.9 synapses/μm^3, see Supplementary Table 2). However, these differences may be due
556 to species and/or age differences (e.g., DeFelipe et al., 1997). In the rat cerebellum, the density
557 of synapses has been previously reported to be 0.8 synapses/μm^3 in the molecular layer
558 (Napper and Harvey, 1988), while our present estimations for the mouse cerebellar cortex
559 range from 0.5 to 0.6 synapses/μm^3 (Supplementary Table 2). Therefore, we currently lack
560 data that are directly comparable to our present estimations, since methodological bias is
561 probably at play in those cases, leaving aside the possible species and age differences.
562 Although work is already in progress on the mouse somatosensory cortex using a methodology
563 that is similar to the one presented here, it would not be practical to wait until results from
564 even a fraction of the 113 subregions examined here become available. Therefore, our
565 calculations must be regarded as reasonable —but provisional— estimations of the minimum
566 densities of glutamatergic synapses in the different brain regions.

567

568 **The size of PSD95 puncta and PSDs.**

569 Regarding the size of puncta and PSDs, what is actually measured in SDM images is different to
570 what is measured after reconstruction of synaptic junctions from serial images obtained by
571 FIB-SEM. In the case of SDM, the images obtained are two-dimensional, so what we actually

572 see is the two-dimensional projection of puncta on the plane of section. Thus, puncta with
573 different orientations will show different apparent surface areas, and only those that are
574 oriented flat with respect to the plane of section will show their true surface area. By contrast,
575 serial images obtained by FIB-SEM allow us to reconstruct the synaptic junctions in 3D. We can
576 then extract the synaptic apposition surface (SAS) from each individual synapse. The SAS
577 represents the surface of apposition between the presynaptic and postsynaptic densities, so
578 the surface area of the SAS is equivalent to the area of the PSD, and we can measure it for
579 every synapse, regardless of its spatial orientation (Morales et al., 2013).

580 One would expect that SDM would underestimate the size of puncta, since most of them will
581 not be flat with respect to the plane of section. In fact, the opposite occurs; SDM imaging
582 clearly overestimates the size of PSD95 puncta when compared with the actual size of PSDs
583 imaged by FIB-SEM (see Figure 8). This can be due to several factors. Light scatter, glare and
584 blur may contribute to the fact that fluorescent puncta appear to be larger than the actual
585 PSDs. The resolution of SDM is also much lower than the resolution of electron microscopy. In
586 the x-y plane, the resolution of SDM was 84 nm/pixel, while FIB-SEM images were acquired at
587 a resolution of 5 nm/pixel. This makes a pixel area of 7056 nm^2 for SDM versus only 25 nm^2 for
588 FIB-SEM. The lower resolution may result in SDM missing the smaller synapses and those that
589 are oriented perpendicularly to the plane of section. Also, the images of several synapses may
590 overlap throughout the thickness of the SDM optical section. This would lead to some puncta
591 in fact being clusters of two or more synapses. In spite of these differences with 3D electron
592 microscopy, the measurements of fluorescent puncta by SDM do distinguish the relative size
593 differences between layers or regions, so they are still useful for the identification and
594 classification of synaptic types (Zhu et al., 2018). Both our SDM and FIB-SEM results indicate
595 that excitatory synapses in SLM are larger than in the SR or SO, in line with previous studies in
596 the rat (Megías et al., 2001).

597 The distribution of synaptic sizes measured from FIB-SEM stacks of images fits a log-normal
598 distribution in the three strata analyzed (see Figure 8 D-F). This trait has also been described in
599 the rat neocortex. This type of distribution is characterized by a skewed curve with a long tail
600 to the right, and it has been found in other synaptic parameters such as synaptic strength,
601 spike transmission probability, and the size of unitary excitatory postsynaptic potentials
602 (Buzsáki and Mizuseki, 2014; Lefort et al., 2009; Song et al., 2005). It is thus tempting to
603 suggest that the size of the synaptic junction is correlated with these and other functional
604 characteristics of the synapse, as has been proposed previously (Santuy et al., 2018b).

605 In summary, it is important to emphasize that acquiring multiple samples at different scales is
606 a highly effective way to obtain a dataset that allows comprehensive analysis of the brain.
607 Since the whole brain cannot be fully reconstructed at the ultrastructural level, it seems clear
608 that only by combining studies at the meso- and nano-scopic levels (light and electron
609 microscopy) can we fully understand the structural arrangement of the brain as a whole [see,
610 for example (Markram et al., 2015), (Kashiwagi et al., 2019)]. Using this strategy, we provide an
611 estimation of the minimum densities of glutamatergic synapses in the different brain regions.
612 These data, in combination with previous studies on the relationship between the connectome
613 and synaptome (Zhu et al., 2018), can be used to identify common and differing principles of
614 synaptic organization. This in turn could serve to further advance efforts to validate and refine
615 realistic brain models.

616

Acknowledgements

This work was supported by grants from the following entities: the Spanish “Ministerio de Ciencia, Innovación y Universidades” (grant PGC2018-094307-B-I00 and the Cajal Blue Brain Project [C080020-09; the Spanish partner of the Blue Brain Project initiative from EPFL, Switzerland]; the European Union’s Horizon 2020 Research and Innovation Programme under grant agreement No. 785907 (Human Brain Project, SGA2); the Wellcome Trust (Technology Development Grant 202932); and the European Research Council (ERC) under the European Union’s Horizon 2020 research and innovation programme (695568 SYNNOVATE). L.T.-R. is a recipient of grants from the EMBO Long-term fellowship 2016–2018 and the IBRO-PERC InEurope grants programme.

References

Anton-Sanchez L, Bielza C, Merchan-Perez A, Rodríguez J-R, DeFelipe J, Larrañaga P (2014) Three-dimensional distribution of cortical synapses: a replicated point pattern-based analysis. Front Neuroanat 8:85.

Aoki C, Miko I, Oviedo H, Mikeladze-Dvali T, Alexandre L, Sweeney N, Bredt DS (2001) Electron microscopic immunocytochemical detection of PSD-95, PSD-93, SAP-102, and SAP-97 at postsynaptic, presynaptic, and nonsynaptic sites of adult and neonatal rat visual cortex. Synapse 40:239–257.

Buzsáki G, Mizuseki K (2014) The log-dynamic brain: how skewed distributions affect network operations. Nat Rev Neurosci 15:264–278.

Chen X, Winters C, Azzam R, Li X, Galbraith JA, Leapman RD, Reese TS (2008) Organization of the core structure of the postsynaptic density. PNAS 105:4453–4458.

Chen X, Winters C, Crocker V, Lazarou M, Sousa AA, Leapman RD, Reese TS (2018) Identification of PSD-95 in the Postsynaptic Density Using MiniSOG and EM Tomography. Front Neuroanat 12.

Colonnier M (1968) Synaptic patterns on different cell types in the different laminae of the cat visual cortex. An electron microscope study. Brain Res 9:268–287.

DeFelipe J, Fairén A (1993) A simple and reliable method for correlative light and electron microscopic studies. J Histochem Cytochem 41:769–772.

DeFelipe J, Marco P, Busturia I, Merchán-Pérez A (1999) Estimation of the number of synapses in the cerebral cortex: methodological considerations. Cereb Cortex 9:722–732.

DeFelipe J, Marco P, Fairén A, Jones EG (1997) Inhibitory synaptogenesis in mouse somatosensory cortex. Cereb Cortex 7:619–634.

DeGiorgis JA, Galbraith JA, Dosemeci A, Chen X, Reese TS (2006) Distribution of the scaffolding proteins PSD-95, PSD-93, and SAP97 in isolated PSDs. Brain Cell Biology 35:239–250.

Farley M, Swulius M, Waxham M (2015) Electron Tomographic Structure and Protein Composition of Isolated Rat Cerebellar, Hippocampal and Cortical Postsynaptic Densities. Neuroscience 304:286–301.

Gray EG (1959) Axo-somatic and axo-dendritic synapses of the cerebral cortex: an electron microscope study. J Anat 93:420–433.

Hafner A-S, Penn AC, Grillo-Bosch D, Retailleau N, Poujol C, Philippat A, Coussen F, Sainlos M, Opazo P, Choquet D (2015) Lengthening of the Stargazin Cytoplasmic Tail Increases Synaptic Transmission by Promoting Interaction to Deeper Domains of PSD-95. Neuron 86:475–489.

Howard CV, Reed MG (2005) Unbiased stereology : three-dimensional measurement in microscopy, 2nd ed. ed. Oxon, UK: Garland Science/BIOS Scientific Publishers.

Husi H, Ward MA, Choudhary JS, Blackstock WP, Grant SGN (2000) Proteomic analysis of NMDA receptor–adhesion protein signaling complexes. Nat Neurosci 3:661–669.

Jeyifous O, Lin EI, Chen X, Antinone SE, Mastro R, Drisdel R, Reese TS, Green WN (2016) Palmitoylation regulates glutamate receptor distributions in postsynaptic densities through control of PSD95 conformation and orientation. PNAS 113:E8482–E8491.

Kashiwagi Y, Higashi T, Obashi K, Sato Y, Komiyama NH, Grant SGN, Okabe S (2019) Computational geometry analysis of dendritic spines by structured illumination microscopy. Nat Commun 10:1285.

Lefort S, Tomm C, Floyd Sarria J-C, Petersen CCH (2009) The Excitatory Neuronal Network of the C2 Barrel Column in Mouse Primary Somatosensory Cortex. Neuron 61:301–316.

Levy JM, Chen X, Reese TS, Nicoll RA (2015) Synaptic Consolidation Normalizes AMPAR Quantal Size following MAGUK Loss. Neuron 87:534–548.

Markram H et al. (2015) Reconstruction and Simulation of Neocortical Microcircuitry. Cell 163:456–492.

Megías M, Emri Z, Freund TF, Gulyás AI (2001) Total number and distribution of inhibitory and excitatory synapses on hippocampal CA1 pyramidal cells. Neuroscience 102:527–540.

Merchán-Pérez A, Rodriguez J-R, Alonso-Nanclares L, Schertel A, Defelipe J (2009) Counting synapses using FIB/SEM microscopy: a true revolution for ultrastructural volume reconstruction. Front Neuroanat 3:18.

Merchán-Pérez A, Rodríguez J-R, González S, Robles V, Defelipe J, Larrañaga P, Bielza C (2014) Three-dimensional spatial distribution of synapses in the neocortex: a dual-beam electron microscopy study. Cereb Cortex 24:1579–1588.

Migaud M, Charlesworth P, Dempster M, Webster LC, Watabe AM, Makhinson M, He Y, Ramsay MF, Morris RGM, Morrison JH, O'Dell TJ, Grant SGN (1998) Enhanced long-term potentiation and impaired learning in mice with mutant postsynaptic density-95 protein. Nature 396:433–439.

Mishchenko Y, Hu T, Spacek J, Mendenhall J, Harris KM, Chklovskii DB (2010) Ultrastructural analysis of hippocampal neuropil from the connectomics perspective. Neuron 67:1009–1020.

Morales J, Alonso-Nanclares L, Rodríguez J-R, DeFelipe J, Rodríguez Á, Merchán-Pérez A (2011) Espina: a tool for the automated segmentation and counting of synapses in large stacks of electron microscopy images. Front Neuroanat 5:18.

Morales J, Rodríguez A, Rodríguez J-R, DeFelipe J, Merchán-Pérez A (2013) Characterization and extraction of the synaptic apposition surface for synaptic geometry analysis. Front Neuroanat 7:20.

Napper RMA, Harvey RJ (1988) Number of parallel fiber synapses on an individual Purkinje cell in the cerebellum of the rat. J Comp Neurol 274:168–177.

Paxinos G, Franklin KB (2004) The mouse brain in stereotaxic coordinates. Gulf Professional Publishing.

Petersen JD, Chen X, Vinade L, Dosemeci A, Lisman JE, Reese TS (2003) Distribution of Postsynaptic Density (PSD)-95 and Ca2+/Calmodulin-Dependent Protein Kinase II at the PSD. J Neurosci 23:11270–11278.

Qiu Z, Yang L, Lu W (2012) A new feature-preserving nonlinear anisotropic diffusion for denoising images containing blobs and ridges. Pattern Recognition Letters 33:319–330.

Roy M, Sorokina O, McLean C, Tapia-González S, DeFelipe J, Armstrong J, Grant S (2018) Regional Diversity in the Postsynaptic Proteome of the Mouse Brain. Proteomes 6:31.

Sadaka Y, Weinfeld E, Lev DL, White EL (2003) Changes in mouse barrel synapses consequent to sensory deprivation from birth. J Comp Neurol 457:75–86.

Sans N, Petralia RS, Wang Y-X, Blahos J, Hell JW, Wenthold RJ (2000) A Developmental Change in NMDA Receptor-Associated Proteins at Hippocampal Synapses. J Neurosci 20:1260–1271.

Santuy A, Rodriguez J-R, DeFelipe J, Merchan-Perez A (2018a) Volume electron microscopy of the distribution of synapses in the neuropil of the juvenile rat somatosensory cortex. Brain Struct Funct 223:77–90.

Santuy A, Rodriguez J-R, DeFelipe J, Merchan-Perez A (2018b) Study of the Size and Shape of Synapses in the Juvenile Rat Somatosensory Cortex with 3D Electron Microscopy. eNeuro 5:e0377-17.2017.

Sassoé-Pognetto M, Utvik JK, Camoletto P, Watanabe M, Stephenson FA, Bredt DS, Ottersen OP (2003) Organization of postsynaptic density proteins and glutamate receptors in axodendritic and dendrodendritic synapses of the rat olfactory bulb: PSD-95/PSD-93 in the Olfactory Bulb. J Comp Neurol 463:237–248.

Schüz A, Palm G (1989) Density of neurons and synapses in the cerebral cortex of the mouse. J Comp Neurol 286:442–455.

Song S, Sjöström PJ, Reigl M, Nelson S, Chklovskii DB (2005) Highly Nonrandom Features of Synaptic Connectivity in Local Cortical Circuits. PLoS Biology 3:e68.

Sorra KE, Fiala JC, Harris KM (1998) Critical assessment of the involvement of perforations, spinules, and spine branching in hippocampal synapse formation. J Comp Neurol 398:225–240.

Swulius MT, Kubota Y, Forest A, Waxham MN (2010) Structure and composition of the postsynaptic density during development. J Comp Neurol 518:4243–4260.

Valtschanoff JG, Burette A, Wenthold RJ, Weinberg RJ (1999) Expression of NR2 receptor subunit in rat somatic sensory cortex: Synaptic distribution and colocalization with NR1 and PSD-95. Journal of Comparative Neurology 410:599–611.

Yamasaki M, Fukaya M, Yamazaki M, Azechi H, Natsume R, Abe M, Sakimura K, Watanabe M (2016) TARP γ-2 and γ-8 Differentially Control AMPAR Density Across Schaffer Collateral/Commissural Synapses in the Hippocampal CA1 Area. J Neurosci 36:4296–4312.

Ye F, Zeng M, Zhang M (2018) Mechanisms of MAGUK-mediated cellular junctional complex organization. Curr Opin Struct Biol 48:6–15.

Zhu F, Cizeron M, Qiu Z, Benavides-Piccione R, Kopanitsa MV, Skene NG, Koniaris B, DeFelipe J, Fransén E, Komiyama NH, Grant SGN (2018) Architecture of the Mouse Brain Synaptome. Neuron 99:781-799.e10.

Zhu J, Shang Y, Zhang M (2016) Mechanistic basis of MAGUK-organized complexes in synaptic development and signalling. Nat Rev Neurosci 17:209–223.